Acta Pharmaceutica Sinica B 2026;16(3):1449−1465

Chinese Pharmaceutical Association
Institute of Materia Medica, Chinese Academy of Medical Sciences

Acta Pharmaceutica Sinica B

www.elsevier.com/locate/apsb
www.sciencedirect.com

ORIGINAL ARTICLE

Inhibition of PGK1 enhances sensitivity to tyrosine kinase inhibitor in T315I-mutant leukemia

Huijing Wang[a,†], Fengyu Jiang[a,†], An Pan[a,†], Chenlong Jin[a], Yangyang Xue[a], Wenjie Liu[c], Renjun Gu[a], Yanyu Zhou[a], Qiuhong Shen[a], Tonghui Ma[a,*], Xiaoxuan Yu[a,b,*]

[a]*School of Medicine, Nanjing University of Chinese Medicine, Nanjing 210023, China*
[b]*State Key Laboratory of Pharmaceutical Biotechnology, School of Life Sciences, Nanjing University, Nanjing 210023, China*
[c]*Department of Hematology, The First Affiliated Hospital of Nanjing Medical University, Jiangsu Province Hospital, Nanjing 210029, China*

Received 5 July 2025; received in revised form 6 September 2025; accepted 28 September 2025

KEY WORDS

PGK1;
Autophagy;
Beclin 1;
Leukemia;
TKI;
VCP;
Flavonoid;
Protein kinase

Abstract Phosphoglycerate kinase 1 (PGK1) is traditionally recognized for its pivotal role in glycolysis. Our findings reveal that PGK1 also functions as a protein kinase phosphorylating valosin-containing protein (VCP) at S746, which subsequently reduces Beclin 1 deubiquitination and impairs autophagy. Inhibition of PGK1 initiates autophagy in T315I-mutant chronic myeloid leukemia (CML) cells, thereby enhancing their sensitivity to first-generation Tyrosine Kinase Inhibitor (TKI) imatinib and third-generation TKI ponatinib. Despite the significant clinical implications, few PGK1-targeting inhibitors have been approved for clinical use to date. Through a comprehensive high-throughput screening of ∼20,000 natural compounds, we identified flavonoid as potent inhibitors of the enzymatic activity of PGK1. Subsequent structural optimization of these flavonoid derivatives led to the development of CPU-216, a compound that binds to the GLU344 and PHE292 residues of PGK1, effectively inhibiting its enzymatic and kinase activity. Notably, CPU-216 induces autophagy *via* VCP and Beclin 1 in CML-T315I cells, enhancing their responsiveness to TKIs. These discoveries propose a novel therapeutic strategy for T315I-mutant CML, underscoring the potential to develop targeted treatments that leverage the kinase functions of PGK1.

*Corresponding authors.
E-mail addresses: xxyu@njucm.edu.cn (Xiaoxuan Yu), matonghui@njucm.edu.cn (Tonghui Ma)
[†]These authors made equal contributions to this work.
Peer review under the responsibility of Chinese Pharmaceutical Association and Institute of Materia Medica, Chinese Academy of Medical Sciences.

https://doi.org/10.1016/j.apsb.2025.12.039

1. Introduction

Tyrosine kinase inhibitors (TKIs) such as imatinib (IM) has shown significant efficacy in treating chronic myeloid leukemia (CML). However, resistance to TKIs emerges in about 40% of patients, with the T315I mutation being particularly troublesome[1,2], accounting for 15%−20% of all resistance-related mutations[3,4]. Ponatinib, a third-generation TKI, despite initial successes in managing the T315I mutation in CML, new challenges have emerged with complex mutations such as G250E/T315I and Y253H/T315I, which are beginning to show resistance to ponatinib[5,6]. Additionally, ponatinib is associated with significant cardiovascular risks and hypertension, underscoring the critical need for the development of alternative treatments that can safely and effectively manage these resistant forms of CML[7,8].

Phosphoglycerate kinase 1 (PGK1) serves as an essential glycolytic enzyme that catalyzes the ATP-generating conversion of 1,3-bisphosphoglycerate (1,3-BPG) to 3-phosphoglycerate (3-PG) through phosphate group transfer to ADP[9-12]. PGK1 overexpression demonstrates significant oncogenic associations, showing strong correlation with aggressive tumor progression and unfavorable clinical outcomes in multiple malignancies, including breast, cervical, hepatic, and pancreatic carcinomas[13]. While its pathological role in T315I-mutated chronic myeloid leukemia requires further investigation, emerging evidence identifies PGK1 as possessing dual enzymatic functions, not only as a glycolytic enzyme but also as a protein kinase [14], though its complete repertoire of phosphorylation targets and regulatory mechanisms remains to be fully elucidated.

Autophagy activation represents a critical mechanism for overcoming TKI resistance in CML, particularly in T315I-mutant cases. Pharmacological modulation of autophagy regulators, including HDAC inhibition (*e.g.*, chidamide) and mTOR blockade (*e.g.*, AZD2014), has demonstrated efficacy in restoring TKI sensitivity through enhanced autophagic flux[15,16]. The betulinic acid-brosimine B hybrid demonstrates synergistic activity with imatinib in CML models, concurrently regulating apoptotic and autophagic pathways[17]. Emerging evidence reveals that PGK1's kinase activity is principally governed by post-translational modifications, particularly through S288 phosphorylation-mediated modulation of its interaction with acetyltransferase ARD1—a critical regulatory mechanism controlling autophagic responses during metabolic stress conditions such as hypoxia or nutrient deprivation. Notably, PGK1 undergoes critical post-translational modifications, including K388 acetylation, which enhances Beclin 1 binding to potentiate both autophagic flux and oncogenic progression. While these observations establish PGK1's kinase-dependent regulation of autophagy, the precise mechanistic underpinnings under normoxic conditions and its direct molecular targets within the autophagic cascade remain to be fully characterized.

Valosin-containing protein (VCP/p97), a ubiquitin-directed ATPases associated with various cellular activities (AAA+) ATPase conserved across species, serves as a central regulator of autophagic machinery[18,19]. Primarily localized in the endoplasmic reticulum (ER), where it is also known as Transitional Endoplasmic Reticulum ATPase (TER ATPase), VCP is integral during the initiation of autophagy[18]. It interacts with the deubiquitinating enzyme Ataxin3 and Beclin 1, facilitating the deubiquitination and subsequent protection of Beclin 1 from degradation[20]. This stabilization permits Beclin 1 incorporation into the PI3K complex, driving Phosphatidylinositol 3-phosphate (PtdIns3P) generation to initiate downstream autophagic cascades[21,22]. VCP further mediates autophagic quality control by facilitating damaged lysosome clearance through coordinated interactions with microtubule-associated protein 1A/1B-light chain 3 (LC3) and sequestosome 1 (SQSTM1) throughout autophagosome biogenesis and maturation[23]. VCP overexpression in murine systems induces pathological LC3 or SQSTM1 accumulation, causing auto-phagosome lysosomal fusion defects and subsequent flux impairment[23-25]. Conversely, inactivation of VCP has been shown to inhibit both autophagosome maturation and autophagic activation, highlighting its essential role in maintaining autophagic balance within cells.

Our findings reveal PGK1 overexpression as a hallmark of T315I-mutated CML resistance, with its genetic suppression restoring TKI sensitivity in refractory cells. Mechanistically, we identified a novel PGK1−VCP phosphorylation axis that drives pro-survival autophagy in resistant populations. Through structure-guided optimization of bioactive flavonoids, we developed CPU-216—a PGK1 inhibitor that potentiates imatinib and ponatinib efficacy in T315I-mutant models by disrupting autophagic flux. This work both elucidates a previously unrecognized resistance mechanism and delivers a translational therapeutic strategy targeting PGK1-dependent autophagy in refractory CML.

2. Materials and methods

2.1. Cell culture and reagents

The human CML cell lines KBM5 and its T315I mutant counterpart, KBM5-T315I, were generously gifted by Dr. Hao Wang at Zhujiang Hospital affiliated with Southern Medical University (Guangzhou, China). These suspension cells were grown in RPMI-1640 culture medium (Gibco, Carlsbad, CA, USA) containing 10% heat-inactivated fetal bovine serum (Life-iLab, Shanghai, China) and a penicillin-streptomycin antibiotic cocktail (100 U/mL). All cell cultures were incubated at 37 °C in a 5% CO_2 atmosphere with controlled humidity. To ensure experimental consistency, only cells passaged within 3 months after thawing were used in the studies.

2.2. Immunohistochemistry (IHC) assay

IHC assay was performed as previously reported[26]. The images were analyzed by ImageJ software.

2.3. Western blot analysis

The cells were harvested and subjected to three washes with phosphate-buffered saline (PBS). Cell lysis was performed using RIPA buffer supplemented with a protease inhibitor cocktail (Yeasen, Shanghai, China, 20124ES03) and phosphatase inhibitors (Yeasen, 20109ES05). After resuspension in an appropriate volume of lysis buffer, the cells were maintained on ice for 50 min with gentle agitation every 25 min to ensure complete lysis. The resulting lysates were then centrifuged at 16,200 × *g* for 30 min at 4 °C to remove cellular debris. Protein concentrations in the supernatants were determined using a BCA protein assay kit (Yeasen, 20201ES76), with optical density measurements obtained using a spectrophotometer.

For immunoblotting analysis, the following primary antibodies were utilized: PGK1 (Abcam, Cambridge, UK, ab154613), VCP (Abcam, ab109240), Caspase-1 (Abways, Shanghai, China, CY5429), Beclin 1 (Abways, Shanghai, China, CY5092), NLRP3 (Santa Cruz Biotechnology, Dallas, TX, USA, SC-518122), SQSTM1/p62 (Abclonal, Wuhan, China, A19700), β-actin (Abcam, ab8226), GSDMD (Abcam, ab219800), HA tag (ProteinTech Group, Rosemont, IL, USA, 51064-2-AP), FLAG tag (Sino Biological, Beijing, China, 101274-mm05t), ubiquitin (ProteinTech Group, 10201-2-AP), and LC3B (Abclonal, A19665).

2.4. Immunofluorescence analysis (IF)

Cells were collected, fixed in cold methanol for 15 min, and permeabilized with 0.2% Triton X-100 (Biofroxx, Einhausen, Germany, 43306) for 30 min. After overnight incubation at 4 °C with the primary antibody (1:200), cells were washed 3 times. The cells were then incubated with Alexa Fluor 488 goat anti-rabbit IgG (H + L) (1:500) or Alexa Fluor 596 goat anti-rabbit IgG (H + L) (1:500) for 1 h at room temperature. The samples were counterstained with DAPI (100 μg/mL) for 10 min at room temperature. Images were captured using a fluorescence microscope.

2.5. Immunoprecipitation−mass spectrometry (IP−MS)

The immunoprecipitation procedure was carried out by first conjugating Protein A/G magnetic beads (MedChemExpress, Monmouth Junction, NJ, USA, HY-K0202) with the target antibodies through a 2-h incubation at 4 °C. Subsequently, the prepared cell lysates were introduced to the antibody-bound beads and allowed to interact overnight under continuous rotation at 4 °C. Following extensive washing with PBST buffer to remove nonspecific binding, the immunocomplexes were eluted in 30 μL of 1 × loading buffer and denatured by heating at 95 °C for 10 min. The immunoprecipitated proteins were then separated by SDS−PAGE and analyzed by Western blotting. For comprehensive protein identification, the excised gel bands were processed for LC−MS/MS analysis at Shanghai Applied Protein Technology Co., Ltd. (China). Using a QExactive high-resolution mass spectrometer (Thermo Fisher Scientific, Waltham, MA, USA), with the acquired mass spectra being matched against the NCBI non-redundant protein sequence database for peptide identification.

2.6. Xenograft tumor growth studies

In this study, immunocompromised male NOD/SCID mice (Gempharmatech Co., Ltd., Nanjing, China), aged 6−9 weeks, were subcutaneously inoculated with KBM5-T315I cells (1×10^7 cells/mouse) to establish xenograft models. Tumor growth was monitored until volumes reached 50−100 mm^3, at which point the animals were randomly allocated into four treatment groups: vehicle control (saline), CPU-216 (20 mg/kg), NG52 (100 mg/kg), and imatinib (100 mg/kg). All treatments were administered *via* intragastric administration every 48 h over a 21-day experimental period. Body weights were recorded biweekly as a general health indicator. Upon completion of the treatment regimen, euthanized mice underwent comprehensive pathological examination, with harvested organs processed for standard hematoxylin−eosin (H&E) histological analysis and tumor specimens immunohistochemically assessed for Ki-67 proliferation marker expression using a specific antibody (ABclonal, A11390).

In this experimental protocol, juvenile female NOD/SCID mice (4−6 weeks old) first underwent sublethal irradiation (1.8 Gy) before receiving intravenous transplantation of primary KBM5-T315I cells through tail vein injection within 24 h post-radiation. After a 7-day engraftment period, the animals were divided into 5 treatment cohorts receiving alternate-day administrations for 4 weeks: vehicle control (normal saline), single-agent CPU-216 (20 mg/kg), NG52 (100 mg/kg), imatinib (100 mg/kg), and combination therapy with reduced-dose CPU-216 (10 mg/kg) plus imatinib (50 mg/kg). The saline-treated group served as both negative control and injection procedure control. Throughout the 28-day treatment period, daily health monitoring was performed. For quantitative analysis of human cell engraftment, peripheral blood samples were collected and stained with anti-human CD45 antibody (Invitrogen, Carlsbad, CA, USA, 58-0459-42) before flow cytometric evaluation. Additionally, bone marrow specimens were obtained for subsequent immunofluorescence microscopic examination.

All animal experiments were conducted in strict compliance with the ethical guidelines for laboratory animals established by China's National Medical Products Administration (NMPA, formerly CFDA). The experimental protocols received full ethical approval from the Institutional Review Board of Nanjing University of Chinese Medicine (Ethics Approval No. 202401A054) before study initiation.

2.7. Reliability analysis

For this investigation, transcriptomic data were retrieved from 2 publicly available GEO repositories (accession numbers GSE245432 and GSE225777). After merging and normalizing the combined datasets, differential expression patterns of PGK1 were computationally analyzed and graphically represented through customized boxplot visualizations generated using the ggpubr package in the R statistical environment.

2.8. Rigid protein−protein docking

To explore potential molecular interactions between VCP and PGK1, we conducted structural docking simulations using the Gramm-X protein−protein docking platform. The three-dimensional structures of both proteins were acquired from multiple structural biology resources, including the UniProt knowledgebase (https://www.uniprot.org), the Protein Data Bank (VCP: P55072; PGK1: P00558), and the AlphaFold protein structure database. Molecular visualization and interaction analysis were subsequently performed using PyMOL molecular graphics system (Version 2.4), which enabled detailed examination of the docking results and generation of high-quality structural representations.

2.9. Drug affinity responsive target stability (DARTS)

Cellular extracts were prepared using standard lysis procedures, with protein concentrations quantified as previously described. The resulting lysates were incubated with either Aloperine (ALO) or phosphate-buffered saline (final concentration $\leq$200 μmol/L) for 90 min at ambient temperature. Following this incubation, protein digestion was initiated by adding pronase (Sigma−Aldrich, St. Louis, MO, USA, catalog number 10165921001) for an additional 30-min treatment period. The processed samples were then separated by sodium dodecyl sulfate-polyacrylamide gel electrophoresis, and protein bands were visualized using a commercial silver staining kit (Solarbio Life Sciences, Beijing, China, product code G7210) in preparation for subsequent mass spectrometric analysis.

2.10. Quantitative real-time PCR

Quantitative real-time PCR (RT-qPCR) was performed as previously reported[27]. The primer sequences were as follows:

GAPDH:
Forward 5′-GCAGGGGGGAGCCAAAAGGG-3′
Reverse 5′-TGCCAGCCCCAGCGTCAAAG-3′
SQSTM1:
Forward 5′-AGATACACCTGCCATGTGCAGC-3′
Reverse 5′-GATCACAGCTCCAAGGAGAACC-3′
MAP1LC3B:
Forward 5′-CTGCTGTGATGTGTAGGAGGAAG-3′
Reverse 5′-GCTGTGAGAGACACATCAGAGC-3′
ATG5:
Forward 5′-TCAGCCACTGCAGAGGTGTTT-3′
Reverse 5′-GGCTGCAGATGGACAGTTGCA-3′
ATG7:
Forward 5′-GGAGATTCAACCAGAGACC-3′
Reverse 5′-GCACAAGCCCAAGAGAGG-3′
ATG12:
Forward 5′-CAGTTTACCATCACTGCCAAAA-3′
Reverse 5′-ACAAAGAAGTGGGCAGTAGAGC-3′

2.11. Immunoprecipitation (IP) analysis

IP assay was performed as previously reported[27]. Immunomagnetic bead conjugates were generated according to the manufacturer's protocol for Protein A/G magnetic beads. Cellular protein extracts were subsequently prepared for immunoprecipitation experiments.

2.12. His-pulldown

Nuclear protein extracts obtained from Flag-PGK1-expressing KBM5-T315I cells were allowed to interact with His-tagged recombinant proteins bound to nickel-charged affinity resin (Ni-NTA-sepharose) during an extended incubation period at 4 °C. Following extensive washing to remove non-specific interactions, the protein complexes retained on the beads were analyzed by Western blotting to detect specific molecular associations.

2.13. Cellular thermal shift assay (CETSA)

Prior to experimental procedures[27], cells were incubated for 6 h with either CPU-216 or DMSO vehicle control. The treated cells were then washed and suspended in ice-cold phosphate-buffered saline (1 mL) supplemented with protease inhibitors, followed by distribution into 100 μL aliquots. These aliquots underwent controlled thermal exposure at predetermined temperatures for precisely 5 min using a calibrated heating block. Immediately after thermal treatment, samples were flash-frozen in liquid nitrogen and subjected to three consecutive freeze-thaw cycles (liquid nitrogen immersion followed by 37 °C water bath incubation) to ensure complete cellular disruption. The lysates were clarified by high-speed centrifugation (12,000 × *g*, 20 min, 4 °C), after which the soluble fractions were mixed with 4 × Laemmli buffer and heat-denatured at 95 °C for 5 min. Protein samples were subsequently separated by SDS−PAGE and transferred to membranes for immunoblot analysis.

2.14. Plasmid transfection and lentiviral infection

The genetic constructs encoding wild-type human PGK1 along with its mutant variants (T378P and K406A), as well as VCP and its phosphorylation-deficient mutants (S478A and S476A), were custom-designed and synthesized by MiaolingBio (Shanghai, China). Additionally, short hairpin RNA (shRNA) sequences targeting PGK1 and VCP were generated for gene silencing applications. For viral transduction, replication-deficient lentiviral particles were produced using a commercial packaging system (Yeasen Biotech, 41102ES10) following the manufacturer's recommended protocol. Target cell populations were transduced with the prepared viral supernatant in the presence of polybrene (Yeasen Biotech, 40804ES76) to enhance infection efficiency. Following transduction, stable cell lines were established through antibiotic selection using puromycin (MedChemExpress, HY-B1743) at appropriate concentrations to eliminate non-transduced cells.

2.15. In vitro kinase assay

The *in vitro* kinase assay was performed using commercially obtained recombinant human PGK1 (Absin, Shanghai, China, ABSO4443) and VCP (Abcam, ab132074) proteins. The enzymatic reactions were conducted in an optimized kinase buffer system (10 mmol/L Tris-HCl pH 7.4, 15 mmol/L NaCl, 10 mmol/L $MgCl_2$, 0.5 mmol/L DTT) with a total reaction volume of 30 μL. Each reaction contained 3 μg of PGK1 as the kinase source, supplemented with ATP and different concentrations of purified VCP substrate. Following a 15-min incubation at physiological temperature (37 °C), the reactions were quenched by adding 2 × Laemmli buffer (Sigma, S3401). Phosphorylation events were subsequently analyzed by immunoblotting using a pan-specific phospho-serine/threonine detection antibody (Abclonal, AP1475) to assess VCP modification status.

2.16. ATP assay

The procedure followed the manufacturer's protocol (Beyotime, Shanghai, China, S0026). Briefly, 100 μL of ATP detection working solution was added to each well or tube and incubated at room temperature for 3−5 min to eliminate background ATP. Next, 20 μL of sample or standard was added, mixed quickly using a pipette, and measured after a 2-s delay with a luminometer or scintillation counter. The sample volume could be adjusted (10−100 μL) based on ATP concentration—higher concentrations required smaller volumes or dilution with lysis buffer. The assay showed linear detection within 1 nmol/L−10 μmol/L ATP.

2.17. Preparation of protein and ligands

The computational analysis was performed using Schrödinger's Maestro molecular modeling platform (v9.7). The initial protein structure was acquired from the Uniport (PGK1: P00558) and subsequently processed through Schrödinger's integrated protein preparation wizard. This preprocessing included elimination of crystallographic water molecules, reconstruction of incomplete side chains, protonation state adjustment, and energy minimization using the OPLS3e force field to resolve atomic clashes. For ligand preparation, compounds from the T001 bioactive compound library were processed through the LigPrep module, generating up to 5 stereochemically diverse conformations per molecule while applying physiological pH constraints (7.0 ± 2.0) for proper ionization state assignment.

2.18. Active site selection with SiteMap

The binding site analysis was conducted using Schrödinger's SiteMap module with optimized parameters for efficient detection of druggable pockets. The algorithm was configured to automatically identify and rank potential binding cavities while creating separate grouping entries for each identified site. Computational efficiency was enhanced through parameter optimization during the search process. The top-scoring binding pocket (designated sitemap_1_site_1) demonstrated the highest predicted druggability with a site score of 1.011, and was consequently selected as the primary binding cavity for subsequent molecular docking studies.

2.19. Grid file preparation

Molecular docking grids were prepared using Schrödinger's Glide module (Maestro v9.7), with the coordinate system centered on the identified sitemap_1_site_1 binding pocket. A cubic grid box with 20 Å edge dimensions was established to encompass the potential ligand binding space, followed by the generation of the corresponding grid parameter file for subsequent docking calculations.

2.20. Virtual screening

The virtual screening protocol was implemented through Schrödinger's Virtual Screening Workflow (Maestro 9.7) with Epik state enumeration enabled. Initial high-throughput screening (HTVS) processed the entire compound library, from which the top 10% hits were advanced to more rigorous docking refinement using both Standard Precision and Extra Precision scoring modes while maintaining default algorithmic parameters. Binding affinities were quantitatively assessed using the XP scoring function, allowing systematic ranking of ligand−protein interactions. Based on these computational predictions, the ten highest-scoring compounds exhibiting superior binding characteristics were prioritized for subsequent experimental validation.

2.21. Kinase panel assay

Kinase profiling against a 217-kinase panel was performed by ICE Bioscience Inc. (Beijing, China) under project NYU-2025050701 using complementary HTRF and ADP-Glo assay platforms. Test compounds (100 × final concentration) were dispensed into 384-well plates *via* acoustic droplet ejection (ECHO system), followed by addition of kinase/Mg^{2+} cocktail (2 ×) and brief centrifugation (1246 × *g*, 1 min). After 10 min pre-incubation at 25 °C, reactions were initiated with ATP/substrate mixture (2 × in kinase buffer) followed by another centrifugation and 60 min incubation. For HTRF detection, terbium cryptate donor (620 nm) and XL665 acceptor (665 nm) emissions were measured on a PHERAstar plate reader, with activity calculated from 665 nm/620 nm ratio. ADP-Glo assays quantified kinase activity through luminescent detection of ADP conversion. All test conditions included 1% DMSO vehicle controls and 10 μmol/L reference inhibitor positive controls, with percentage inhibition calculated as Eq. (1):

$$\text{Inhibition}\,(\%) = \left\lfloor 1 - \frac{\overline{\text{Data}}_{\text{Cmpd}} - \overline{\text{Data}}_{\text{positive}}}{\overline{\text{Data}}_{\text{vehicle}} - \overline{\text{Data}}_{\text{positive}}} \right\rfloor \times 100 \quad (1)$$

$\overline{\text{Data}}_{\text{positive}}$: The average ratio for the positive controls (10 μmol/L positive control article); $\overline{\text{Data}}_{\text{vehicle}}$: The average ratio for the vehicle controls (1% DMSO).

The kinase selectivity profile was determined through comprehensive screening against 80 kinase targets using ADP-Glo and HTRF assay platforms. A visual representation was generated where each kinase target is marked by a colored data point corresponding to its inhibition level: deep red (90%−100% inhibition), orange (80%−90%), blue (70%−80%), light blue (50%−70%), and green (<50% inhibition). This heatmap-style analysis provides immediate visualization of compound specificity, enabling clear identification of primary therapeutic targets (high inhibition clusters) and potential off-target interactions (lower inhibition groups), information essential for both efficacy optimization and safety profiling during lead compound development.

2.22. Statistical analysis

Experimental results are expressed as mean values ± standard error of the mean (SEM), derived from 3 biologically independent replicates. For datasets involving multiple experimental groups, statistical significance was assessed through one-way ANOVA with Bonferroni's *post hoc* correction. Pairwise comparisons were evaluated using two-tailed Student's *t*-tests. Thresholds for statistical significance were established at $^{*}P < 0.05$ (significant) and $^{**}P < 0.01$ (highly significant).

3. Results

3.1. PGK1 inhibition enhances the sensitivity of T315I-mutant CML to TKI

In our investigation of the role of PGK1 in T315I resistance in CML, we analyzed differentially expressed genes in CML cells with and without the T315I mutation, utilizing the GSE245432 and GSE225777 databases. Our findings revealed a significant increase in PGK1 expression in T315I-mutated CML cells compared to non-mutant counterparts (Fig. 1A). Subsequently, experimental validation was performed in both KBM5 and KBM5-T315I cell lines, with the results demonstrating concordance with the database findings (Fig. 1B). To further explore the function of PGK1 in T315I-mutated CML, we generated PGK1 knockdown and overexpression cell lines in KBM5-T315I cells. Western blot analysis confirmed the successful transfection (Fig. 1C). The effect of PGK1 modulation on the proliferative capacity of KBM5-T315I cells was evaluated using CCK-8, which showed that PGK1 knockdown reduced cell viability, while

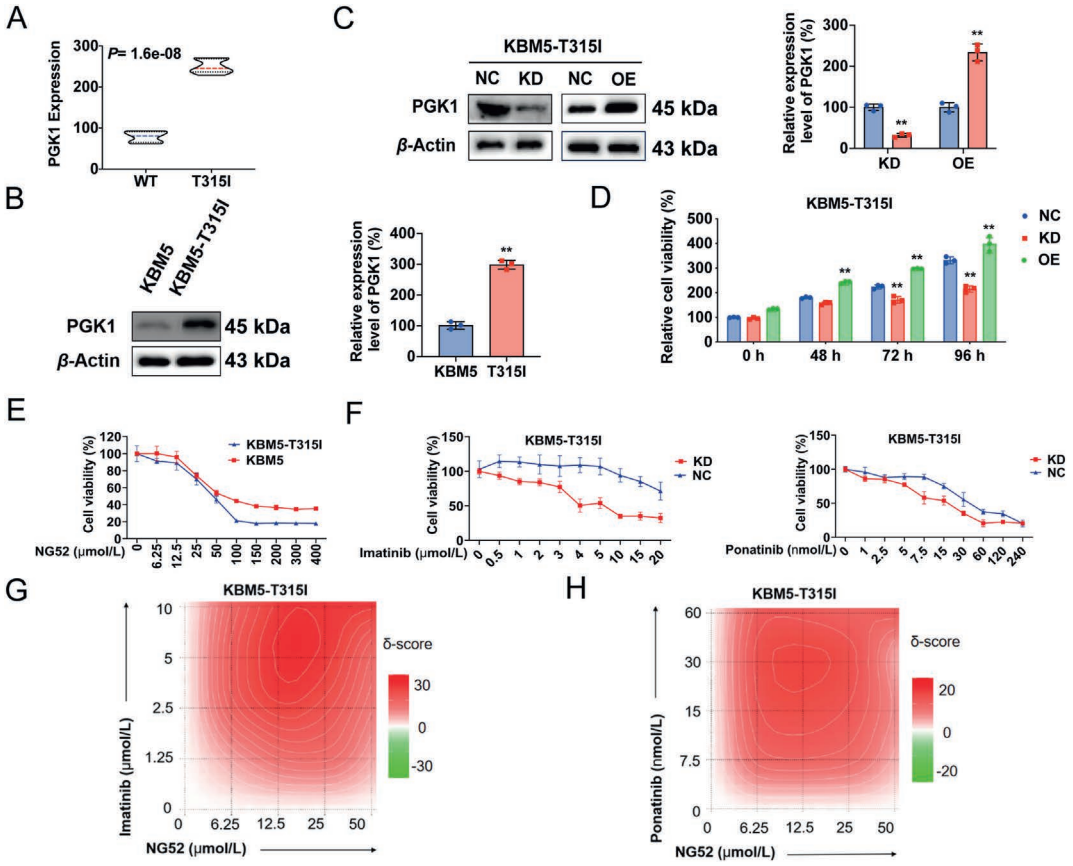

Figure 1 PGK1 inhibition enhances the sensitivity of T315I-mutant CML to TKI. (A) The expression of PGK1 in T315I mutant and non-mutant CML patients was analyzed. (B) Western blot analysis assessed the expression of PGK1 in KBM5 and KBM5-T315I. (C) Western blot analysis assessed the overexpression of PGK1 (OE) and the knockdown efficiency of shPGK1 (KD) compared to the empty vector control (NC) in KBM5-T315I cells. (D) Cell viability of KBM5-T315I-PGK1 KD and OE cells was measured at 48, 72, and 96 h using the CCK-8 assay, compared to NC cells. (E) KBM5-T315I and KBM5 cells were treated with 0−400 μmol/L NG52 for 24 h, and cell viability was assessed using the CCK-8 assay. (F) KBM5-T315I and KBM5-T315I-PGK1-KD cells were treated with imatinib and ponatinib for 24 h, and cell viability was assessed using the CCK-8 assay. (G, H) The combined effect of NG52 with imatinib or ponatinib on KBM5-T315I viability was evaluated after 24 h using the CCK-8 assay. Synergy score (*δ*-score) analysis was conducted using the web application SynergyFinder (https://synergynder.fimm.fi), Synergy score>10: synergy; <−10: antagonism. Error bars: SEM, $n = 3$. Statistical significance of differences in mean values: $^{**}P < 0.01$.

overexpression promoted it (Fig. 1D). Building on these findings, we assessed the inhibitory effect of the PGK1 inhibitor NG52 on KBM5-T315I and KBM5. The results showed a better inhibitory effect on KBM5-T315I (Fig. 1E).

TKIs, such as imatinib and ponatinib, are primary treatments for CML. We assessed the impact of these TKIs on the viability of KBM5-T315I cells following PGK1 knockdown. The results demonstrated that PGK1-knockdown cells exhibited increased sensitivity to imatinib and ponatinib, suggesting that PGK1 inhibition may enhance the responsiveness of T315I-mutant CML to TKI therapy (Fig. 1F). Additionally, we assessed the synergistic effects of TKIs and NG52 by measuring cell viability at varying concentration ratios using the CCK-8 assay in KBM5 and KBM5-T315I after 24 h (Fig. 1G). SynergyFinder analysis revealed that NG52 and imatinib exhibited strong synergy in KBM5-T315I (synergy score: 16.63). In contrast, no significant synergy was observed in KBM5 cells, with imatinib high-dose groups even showing antagonism (synergy score: −7.32). Furthermore, NG52 sensitized T315I-mutant cells to ponatinib, demonstrating synergistic effects with a synergy score of 10.11 (Fig. 1H). These findings highlight the therapeutic potential of combining TKIs with PGK1 inhibition for T315I-mutant CML.

3.2. *PGK1 interacts with VCP*

To elucidate the role of PGK1 in T315I-mutated CML, we employed IP−MS to identify proteins that directly interact with PGK1 in KBM5-T315I cells (Supporting Information Fig. S1). This analysis revealed a direct interaction between PGK1 and VCP, as evidenced by specific peptides shown in Fig. 2A. The interaction was further validated by co-IP in the same cell line (Fig. 2B) and in HEK293T cells, demonstrating significant complex formation between Flag-tagged PGK1 and HA-tagged VCP (Fig. 2C). The direct binding was additionally confirmed *in vitro* using GST pull-down assays with recombinant GST-VCP and His-tagged PGK1 proteins (Fig. 2D).

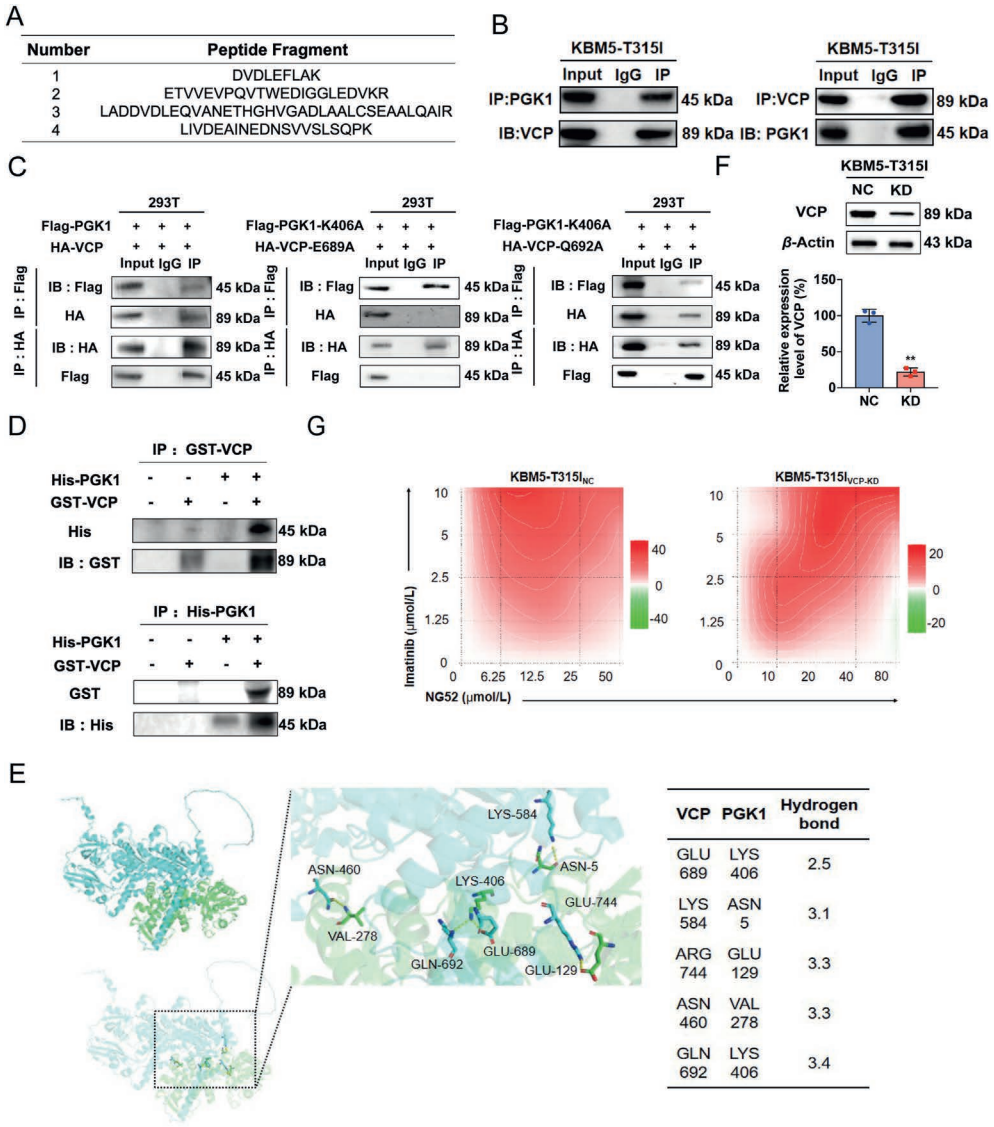

Figure 2 PGK1 interacts with VCP. (A) Immunoprecipitation (IP) combined with LC-MS/MS was used to identify PGK1 binding proteins, as well as the protein profiles and peptide segments of VCP. (B) Co-immunoprecipitation (Co-IP) assays were performed to investigate the interaction between PGK1 and VCP proteins in KBM5-T315I cells. (C) HEK-293T cells were transfected with Flag-PGK1/Flag-PGK1-K406A and HA-VCP/HA-VCP-E689A/HA-VCP-Q692A. Cell extracts were immunoprecipitated using anti-HA and anti-Flag antibodies, followed by immunoblotting. (D) Pulldown assays were conducted with His-PGK1 and GST-VCP proteins. Western blotting was performed using the indicated antibodies. (E) Rigid protein−protein docking between VCP (blue) and PGK1 (green) was performed using GRAMM-X software to investigate the interaction between the two proteins. The protein structures were obtained from the Uniprot, PDB, and Alphafold databases. (F) Western blot analysis assessed the knockdown efficiency of shVCP (KD) compared to the empty vector control (NC) in KBM5-T315I cells. Error bars: SEM, $n = 3$. Statistical significance of differences in mean values: $^{**}P < 0.01$. (G) The combined effect of NG52 with imatinib on cell viability was evaluated after 24 h in VCP-KD-KBM5-T315I cells using the CCK-8 assay. Synergy score (δ-score) analysis was conducted using the web application SynergyFinder (https://synergynder.fimm.fi). Synergy score>10: synergy; <−10: antagonism.

Furthermore, to explore the specific binding sites between VCP and PGK1, we utilized GRAMM-X for analysis and prediction. The interaction model showed PGK1 forming hydrogen bonds with VCP through some residues, represented by a yellow dashed line, indicating a stable protein docking model (Fig. 2E). Structurally, VCP comprises an N-terminal region, D1 ATPase domain, D2 ATPase domain, and C-terminal region. Gramm-X docking simulations revealed 14 potential hydrogen bonds between PGK1 and VCP, with 12 localized in the D2 ATPase domain, underscoring its pivotal role in their interaction. Ranking the docking sites demonstrated that PGK1-Lys406 and VCP-Glu689 exhibited the closest proximity, with PGK1-Lys406 potentially interacting additionally with VCP-Glu692 adjacent to Glu689. Subsequent co-IP assays using PGK1-Lys406 and VCP-Glu689/Glu692 mutants confirmed hydrogen bond formation between PGK1-Lys406 and VCP-Glu689, which is in the D2 domain (Fig. 2C).

To further validate the pivotal role of VCP in PGK1 inhibition-mediated TKI sensitization, we established VCP-knockdown

(VCP-KD) KBM5-T315I cells and transfection efficiency shown in Fig. 2F. Moreover, the synergy score for NG52 and imatinib in VCP-KD cells was 7.57, markedly different from the NC group, 15.66. These findings conclusively demonstrate that VCP is essential for the effects of PGK1 targeting and TKI sensitization in KBM5-T315I cells (Fig. 2G).

3.3. *PGK1 phosphorylates VCP at Ser 746*

PGK1 is well-established as a key glycolytic enzyme, we first sought to determine whether its function in KBM5-T315I cells depends on glycolysis. We examined the effects of NG52 on lactate dehydrogenase (LDH) production, a key glycolytic output. NG52 (6.25−50 μmol/L), at concentrations that induced growth inhibition and potentially enhanced imatinib efficacy in KBM5-T315I cells, showed no significant effect on LDH levels, suggesting that the pharmacological activity of NG52 is independent of glycolytic inhibition (Fig. 3A). To exclude the influence of PGK1 on glycolysis, we inhibited pyruvate kinase, the downstream enzyme catalyzed by PGK1 in glycolysis. There are 2 types of pyruvate kinase: PKM1 is primarily expressed in terminally differentiated cells with high energy demands, such as muscle and brain, while PKM2 is mainly expressed in tissues with strong anabolic demands, such as tumor cells, and is associated with the Warburg effect, exhibiting weaker metabolic regulatory activity[28]. Therefore, we selected the PKM2-IN-1 to inhibit PKM2. Results showed that at an effective inhibitory dose of PKM2 (3 μmol/L), PKM2-IN-1 did not affect the proliferation of KBM5-T315I cells (Fig. 3B) or sensitize them to imatinib, with a synergy score of −4.49. Pretreating KBM5-T315I cells with 3 μmol/L PKM2-IN-1 did not alter the synergistic effect of NG52 and imatinib (synergy score: 15.16).

Subsequent investigations focused on the kinase activity of PGK1. We constructed a kinase-deficient mutant, T378P[29], of PGK1 and performed *in vitro* kinase assays with VCP (Fig. 3C). These assays, using either purified recombinant His-PGK1 or His-PGK1-T378P, showed that VCP was phosphorylated by His-PGK1 but not by the mutant, as detected by a pan-phosphorylation antibody, confirming the specific phosphorylation of VCP (Fig. 3D and E). Additionally, a reduction in VCP phosphorylation levels was observed upon co-incubation of KBM5-T315I cells with the PGK1 inhibitor NG52, further indicating direct phosphorylation by PGK1 (Fig. 3F). We also examined the effects of PGK1 overexpression, knockout, and

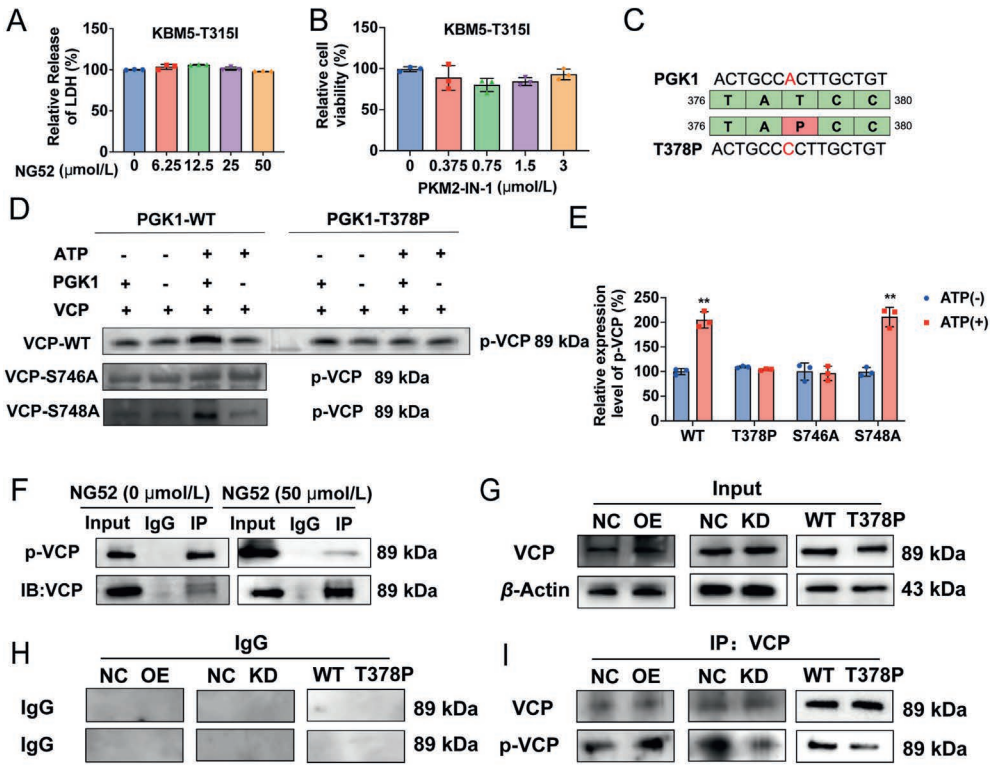

Figure 3 PGK1 phosphorylates VCP at Ser 746. (A) Lactate production in KBM5-T315I cells after treatment with NG52 (0, 6.25, 12.5, 25, 50 μmol/L) for 24 h. (B) Cell viability changes in KBM5-T315I cells after treatment with PKM2-IN-1 (0, 0.375, 0.75, 1.5, 3 μmol/L) for 24 h, as detected by CCK-8 assay. (C) Flowchart illustrating the kinase-deficient mutant of PGK1 (T378P). (D, E) Phosphorylation reactions of VCP protein, PGK1-WT, and PGK1-T378P, VCP-WT, VCP-S746A, VCP-S748A in the presence or absence of ATP were conducted in a defined system. VCP phosphorylation was detected using a pan-phospho-serine/threonine antibody. (F) KBM5-T315I cells were treated with 50 μmol/L NG52 for 24 h. Cells were then immunoprecipitated with an anti-VCP antibody, followed by Western blot analysis. Phosphorylation was detected using a pan-phospho-serine/threonine antibody. (G−I) PGK1-OE and PGK1-KD cells were immunoprecipitated with an anti-VCP antibody, followed by Western blot analysis. Phosphorylation was detected using a pan-phospho-serine/threonine antibody; PGK1-KD cells were transfected with PGK1-WT cDNA or PGK1-T378P cDNA. WT and T378P cells were immunoprecipitated with an anti-VCP antibody, followed by Western blot analysis. Phosphorylation was detected using a pan-phospho-serine/threonine antibody. Error bars: SEM, $n = 3$. Statistical significance of differences in mean values: $^{**}P < 0.01$.

kinase-deficient mutations in KBM5-T315I cells on VCP phosphorylation. The results demonstrated increased VCP phosphorylation in PGK1-overexpressing cells (OE) compared to wild-type (WT), while PGK1 knockdown (KD) and kinase-deficient mutants showed reduced VCP phosphorylation (Fig. 3G−I). These results underscore the pivotal role of PGK1 kinase activity in modulating phosphorylation events within this cellular context.

Since PGK1 is a serine/threonine kinase, we focused primarily on its serine/threonine phosphorylation sites rather than tyrosine. Indeed, multiple phosphorylation sites in VCP (Ser7, Thr76, Ser352, Ser746, Ser748, Ser784, and Tyr805) have been reported[30-36]. Results revealed that Lys406 of PGK1 forms hydrogen bonds with Glu689 of VCP, suggesting that phosphorylation sites may reside near the binding interface. Therefore, we focused more on the D2 region, particularly the sites near Glu689. Notably, prior studies indicate that phosphorylation of VCP at Ser746 and Ser748 regulates its association with ubiquitinated proteins[33], consistent with our finding that VCP phosphorylation influences autophagy. Subsequent *in vitro* kinase assays confirmed that PGK1 phosphorylates VCP at Ser746 instead of Ser748 (Fig. 3D).

3.4. Inhibition of PGK1 induces autophagy in T315I-mutant CML cells by increasing the deubiquitination of Beclin 1

In subsequent studies using KBM5-T315I cells, we investigated how VCP phosphorylation modulates autophagy. We examined whether PGK1-mediated phosphorylation of VCP affects autophagic activity in these cells. In PGK1-KD and PGK1-OE cells, we observed elevated levels of LC3B-II and Beclin 1 upon PGK1 knockdown, whereas their expression decreased in PGK1-overexpressing cells (Fig. 4A and B), suggesting that PGK1 suppression promotes autophagy in KBM5-T315I cells. Notably, cells expressing the PGK1-T378P mutant exhibited higher LC3B-II and Beclin 1 levels than those expressing wild-type PGK1, further supporting that impaired VCP phosphorylation enhances autophagy (Fig. 4A and B). Since Beclin 1 is essential for autophagy initiation and can be regulated by VCP-mediated deubiquitination, we performed co-IP assays and confirmed an interaction between VCP and Beclin 1 (Fig. 4C). Pharmacological inhibition of PGK1 kinase activity with NG52 reduced VCP phosphorylation, leading to decreased Beclin 1 ubiquitination and increased protein expression (Fig. 4D). Consistent with these findings, transmission electron microscopy revealed a marked increase in autophagic vesicles in NG52-treated KBM5-T315I cells (Fig. 4E), further corroborating the role of PGK1−VCP signaling in autophagy regulation. Protein assays revealed that NG52 treatment increased Beclin 1 expression and the LC3B-II/LC3B-I ratio, while simultaneously reducing SQSTM1 expression in a dose-dependent manner (Fig. 4F and G). Additionally, flow cytometry showed an increase in autophagy in NG52-treated KBM5-T315I cells (Fig. 4H), and RT-qPCR demonstrated upregulation of autophagy-related genes *ATG5, ATG7*, *ATG12*, and *MAP1LC3B*, with a concomitant decrease in *SQSTM1* expression (Fig. 4I and J). Furthermore, by transfecting KBM5-T315I cells with GFP-LC3B, we found that NG52 could promote the formation of LC3 puncta. Intriguingly, this increase in the number of LC3 puncta could be reversed by DBeQ, an inhibitor of VCP (Fig. 4K), indicating a specific modulatory function of VCP in this context. Given that breakpoint cluster region-abelson murine leukemia viral oncogene homolog 1 (BCR-ABL) is the key oncogenic driver in CML, we next examined the impact of PGK1 inhibition on BCR-ABL protein levels. Treatment with NG52 reduced BCR-ABL expression in a dose-dependent manner, an effect that was reversed by the autophagy inhibitor 3-MA. Furthermore, genetic ablation of PGK1 decreased BCR-ABL levels, while PGK1 overexpression enhanced them. Notably, cells expressing the phospho-deficient PGK1-T378P mutant exhibited reduced BCR-ABL expression, suggesting that BCR-ABL serves as a critical autophagic degradation substrate downstream of the PGK1−VCP axis (Fig. 4L and M).

3.5. Chemical screening led to the identification of CPU-216, which directly binds to PGK1, inhibiting its enzymatic activity and enhances their sensitivity to TKI

In our search for effective inhibitors of PGK1, we conducted a high-throughput screen of a library containing Food and Drug Administration (FDA)-approved small molecules and approximately 12,000 natural compounds using Schrödinger software. From this, we selected the top 10 compounds with the highest docking scores for PGK1 enzymatic activity by ATP production in HEK-293T cells and ultimately identified the flavonoid compound 10 as a potential inhibitor (Fig. 5A and B and Supporting Information Table S1). Following structural modifications of these flavonoids and further testing, we discovered that CPU-216 (Compound **13**, Supporting Information Fig. S2) significantly reduced PGK1 enzymatic activity in a dose-dependent manner, demonstrating potent inhibition (Fig. 5C and D). We further evaluated the inhibitory effect of CPU-216 on PGK1 kinase activity. As demonstrated by VCP phosphorylation assays, CPU-216 (0−0.5 μmol/L) significantly suppressed PGK1 enzymatic activity (Fig. 5E). Then, the kinase selectivity profile of CPU-216 (0.5 μmol/L) was evaluated using the ICEKP Kinome Panel comprising 80 kinase activity assays. Results demonstrated that while CPU-216 showed weak inhibitory effects on other kinases, it exhibited potent and selective inhibition of PGK1 enzymatic activity (Fig. 5F).

To further elucidate the cellular targets of CPU-216 in KBM5-T315I cells, we employed the DARTS assay. This ligand independent assay revealed a direct interaction between PGK1 and CPU-216 (Fig. 5G), which was corroborated by the cellular thermal shift assay, confirming that CPU-216 physically engaged PGK1 and stabilized it against thermal denaturation (Fig. 5H). Additionally, the assay showed that CPU-216 reduced the pronase-induced degradation of PGK1 in a concentration-dependent manner (Fig. 5I). Microscale thermophoresis further demonstrated that CPU-216 increased the thermal stability of PGK1 (Fig. 5J). Molecular docking studies conducted using Schrödinger software suggested that CPU-216 binds directly to the GLU344 and PHE292 residues on PGK1. These results provide a molecular basis for the inhibitory mechanism of CPU-216 on PGK1 and suggest a targeted approach for improving therapeutic strategies in the treatment of CML with the T315I mutation (Fig. 5K).

We next evaluated the growth-inhibitory effects of CPU-216 on CML cells. After 12 h of treatment, CPU-216 showed potent growth inhibition in CML cells, with significantly lower IC_{50} values in T315I-mutant cells (KBM5-T315I: 5.88 ± 1.67 μmol/L *versus* KBM5: 17.63 ± 3.72 μmol/L) (Fig. 5L). Furthermore, we assessed the effects of CPU-216 on KBM5-T315I cells with PGK1 knockdown, overexpression, or the T378P mutation. PGK1

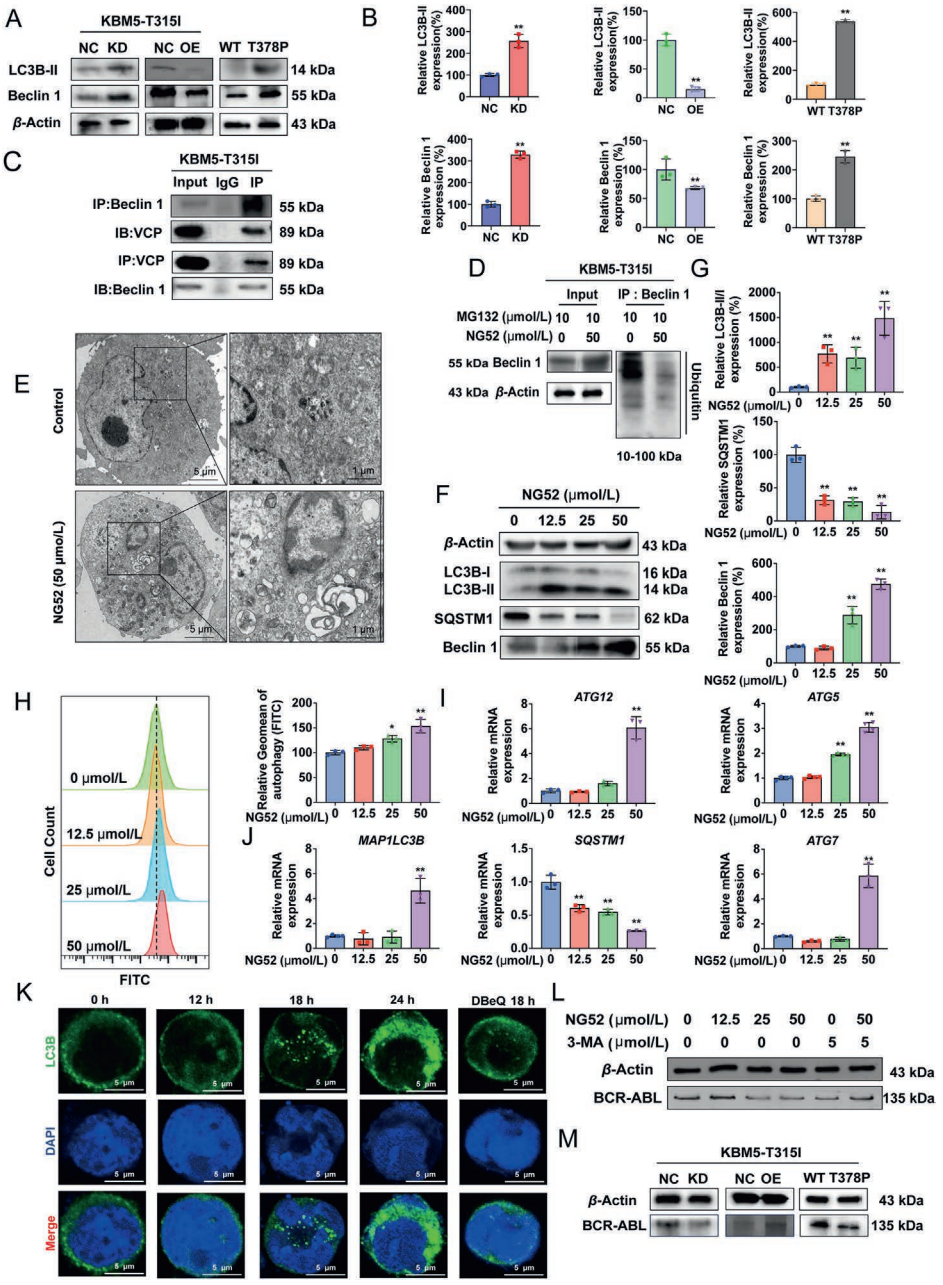

Figure 4 Inhibition of PGK1 induces autophagy in T315I-mutant CML cells by increasing the deubiquitination of Beclin 1. (A, B) Expression levels of LC3B-II and Beclin 1 were analyzed by Western blot in PGK1-OE, PGK1-KD, PGK1-T378P cells, β-actin was used as a loading control. (C) Co-IP experiments demonstrated an interaction between VCP and Beclin 1. (D) Western blot analysis of the level of ubiquitination in KBM5-T315I cells treated with NG52 (50 μmol/L) and 10 μmol/L MG132 for 24 h. (E) Transmission electron microscopy (TEM) was used to observe lysosomal morphology following treatment with 50 μmol/L of NG52. (F, G) The expression levels of autophagy-related proteins under different concentrations of NG52 treatment. (H) Flow cytometric analysis of fluorescence intensity values of autophagy and GEOmean analysis. (I, J) Transcriptional expression of autophagy-related genes under different concentrations of NG52 treatment. (K) The effect of NG52 on LC3B accumulation in KBM5-T315I cells at different time points. (L) The expression levels of BCR-ABL were analyzed by Western blot in KBM5-T315I cells after NG52 (0, 12.5, 25, 50 μmol/L) treatment for 24 h in the presence or absence of 5 mmol/L 3-MA, β-actin was used as a loading control. (M) Expression levels of BCR-ABL were analyzed by Western blot in PGK1-OE, PGK1-KD, and PGK1-MT cells, β-actin was used as a loading control. Error bars: SEM, $n \geq 3$. Statistical significance of differences in mean values: $^{*}P < 0.05$, $^{**}P < 0.01$.

knockdown and the T378P mutation attenuated CPU-216-induced growth inhibition, while PGK1 overexpression enhanced it, indicating that CPU-216 acts through PGK1 (Fig. 5M). Since prior studies have shown that PGK1 interacts with VCP, we next examined the impact of CPU-216 in VCP-knockdown cells rescued with either wild-type VCP or the E689A mutant. Compared to wild-type, the E689A mutant significantly reduced the growth-inhibitory effects of CPU-216 (Fig. 5N).

In subsequent analyses, we explored the potential synergistic effects of TKIs and CPU-216 on the viability of KBM5-T315I cells.

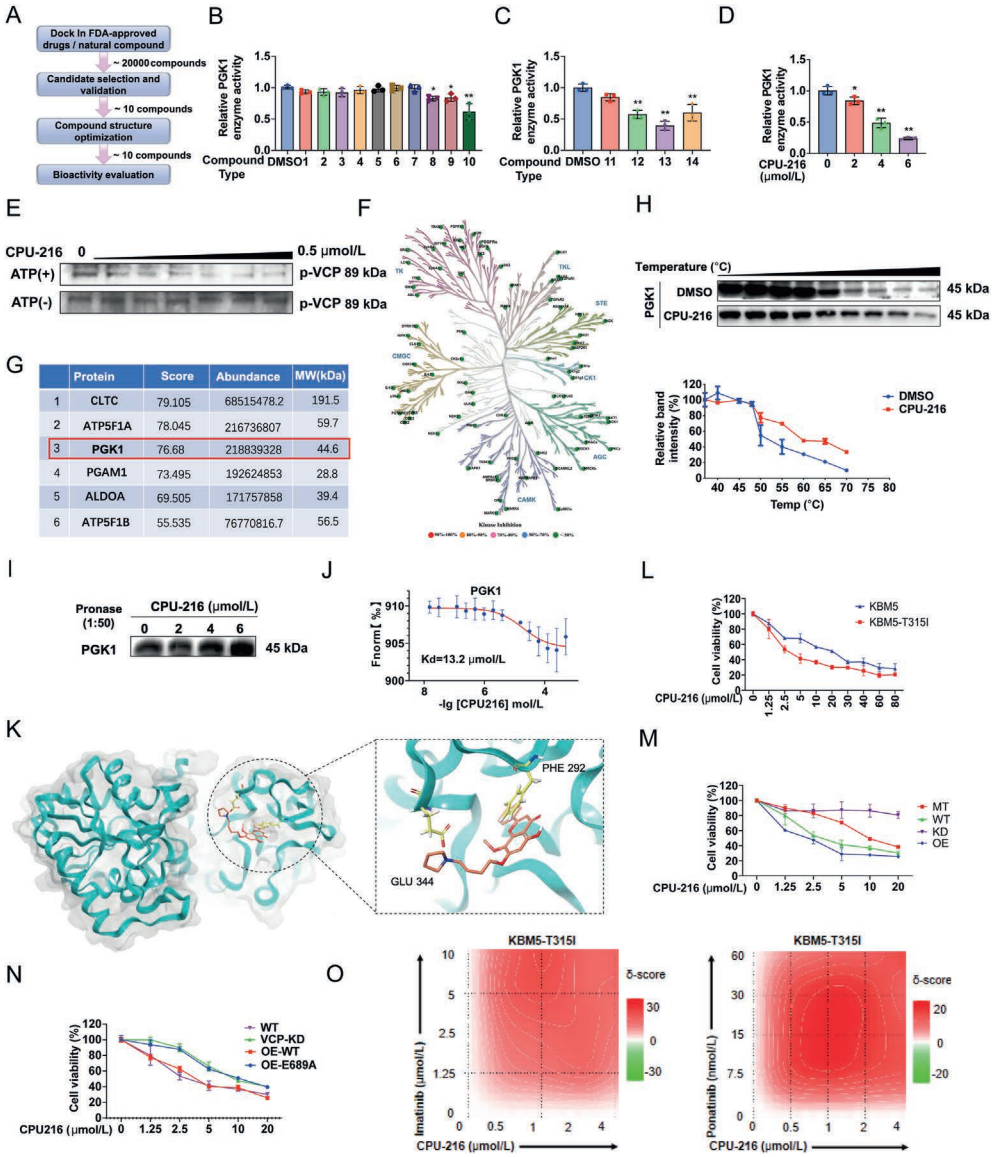

Figure 5 Chemical screening and identification of CPU-216 directly bound to PGK1. (A) A summary of the search for small molecular compounds that target PGK1. (B) Inhibition of ATP production by candidate molecules at 10 μmol/L for 12 h in HEK-293T. (C) ATP production activity was assessed by adding various synthetic derivatives of flavonoids individually 6 μmol/L for 12 h in HEK-293T. (D) The ATP production of CPU-216 (0, 2, 4, 6 μmol/L) in HEK-293T at 12 h. (E) The inhibitory effect of CPU-216 (0, 7.8125, 15.625, 31.25, 62.5, 125, 250, 500 nmol/L) on PGK1 enzyme activity. (F) The kinase profiling selectivity investigation of CPU-216 at a concentration of 0.5 μmol/L was carried out by ICE Bioscience using the ICEKP Kinome Panel, based on 80 kinase activity assays. (G) Direct binding of PGK1 to CPU-216. (H) CETSA melt curve of PGK1 in KBM5-T315I cells, with and without the presence of CPU-216 (6 μmol/L), after heat treatment. (I) Immunoblot analysis of PGK1 in KBM5-T315I cells treated with 0, 2, 4, and 6 μmol/L CPU-216 and pronase (1:50). (J) The interaction between CPU-216 and PGK1 was detected by Microscale Thermophoresis (MST). (K) Molecular docking analysis of CPU-216 and PGK1. (L) CML cells were treated with 0−80 μmol/L CPU-216 for 12 h, and cell viability was assessed using the CCK-8 assay. (M) KBM5-T315I-PGK1-WT, PGK1-OE, PGK1-KD, and PGK1-T378P cells were treated with 0−80 μmol/L CPU-216 for 12 h, and cell viability was assessed using the CCK-8 assay. (N) KBM5-T315I-VCP-KD cells were transfected with VCP-WT cDNA or VCP-E689A cDNA. WT and E689A cells were treated with 0−80 μmol/L CPU-216 for 12 h, and cell viability were assessed using the CCK-8 assay. (O) The effects of CPU-216 combination with imatinib or ponatinib, on the growth and viability of KBM5-T315I cells. Synergy score (δ-score) >10: synergy; <−10: antagonism. Error bars: SEM, $n = 3$. Statistical significance of differences in mean values: $^{*}P < 0.05$, $^{**}P < 0.01$.

Using the CCK-8 assay, we assessed cell viability after 12 h of exposure to various concentration ratios of TKIs and CPU-216. Our findings revealed a pronounced synergistic effect; the combination index for CPU-216 and imatinib was 14.45, while CPU-216 and ponatinib was 13.41 (Fig. 5O).

3.6. CPU-216 induces autophagy in T315I-mutant CML cells

Given the significant role of PGK1 in the autophagy of T315I-mutant CML, we further investigated the morphological effects of CPU-216 on KBM5-T315I cells using transmission electron

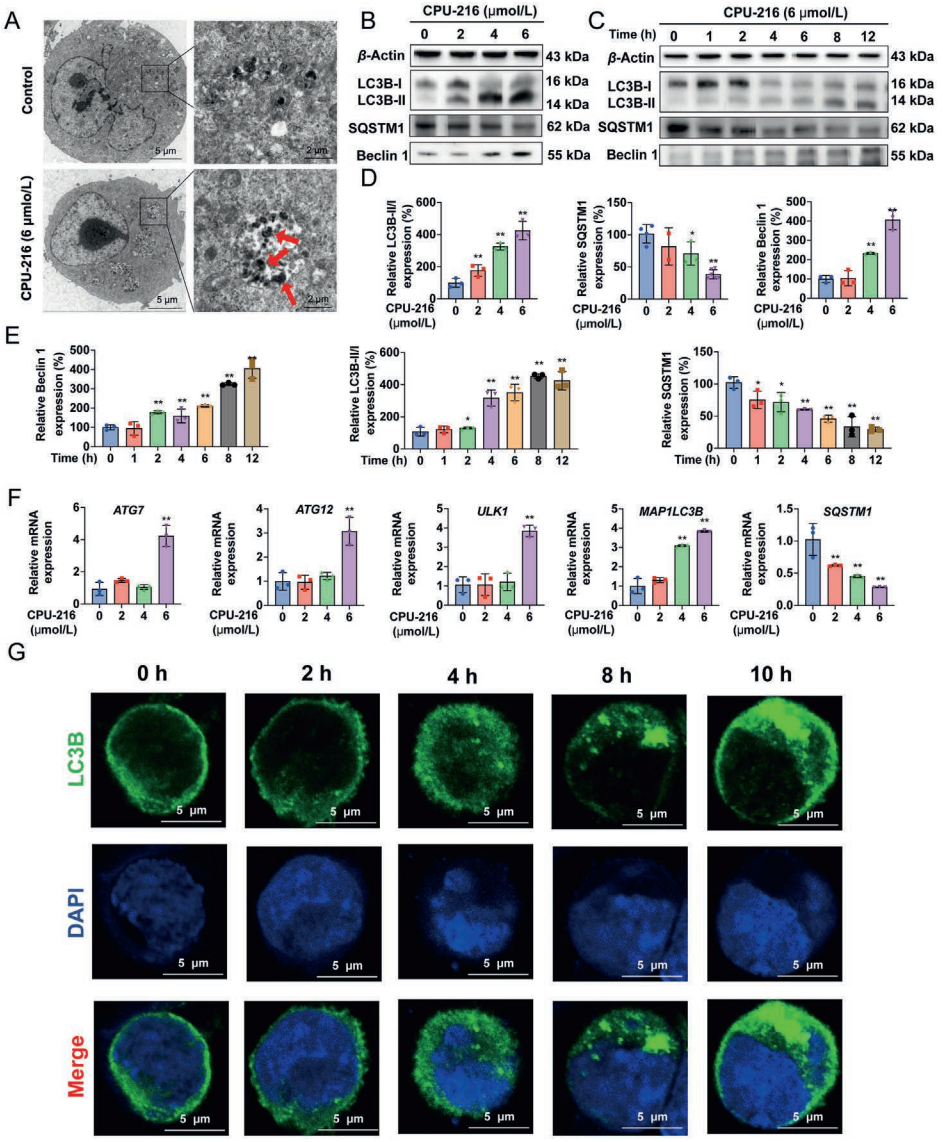

Figure 6 CPU-216 induces autophagy in KBM5-T315I cells. (A) Transmission electron microscopy was used to observe lysosomal morphology after treatment with 6 μmol/L CPU-216. (B, D) Expression levels of autophagy-related proteins LC3B, SQSTM1, and Beclin 1 following treatment with various concentrations of CPU-216 (0, 2, 4, 6 μmol/L) for 12 h, β-actin was used as a loading control. (C, E) Expression of autophagy-related proteins LC3B, SQSTM1, and Beclin 1 at various time points (0, 1, 2, 4, 6, 8, 12 h) after treatment with 6 μmol/L CPU-216, β-actin was used as a loading control. (F) Expression of autophagy-related genes *ATG7*, *ATG12*, *ULK1*, *MAP1LC3B*, and *SQSTM1* following treatment with different concentrations of CPU-216 (0, 2, 4, 6 μmol/L) for 12 h. (G) The effect of 6 μmol/L CPU-216 on LC3B accumulation in KBM5-T315I cells at different time points. Error bars: SEM, $n = 3$. Statistical significance of differences in mean values: $^{*}P < 0.05$, $^{**}P < 0.01$.

microscopy. Notably, an increased number of autophagic vesicles was observed in CPU-216-treated cells (Fig. 6A). Additionally, Beclin 1 levels and the LC3B-II/LC3B-I ratio increased in a time- and dose-dependent manner, while SQSTM1 expression decreased (Fig. 6B–E). RT-qPCR experiments confirmed the upregulation of autophagy-related gene *ATG7*, *ATG12*, *ULK1*, and *MAP1LC3B*, and the downregulation of *SQSTM1*, which aligned with the protein level results (Fig. 6F). Furthermore, we evaluated the effect of CPU-216 on autophagy activity in cells overexpressing wild-type VCP *versus* the VCP-E689A mutant. CPU-216 effectively promoted autophagy in wild-type VCP cells, whereas these effects were attenuated in mutant VCP-expressing CML cells (Supporting Information Fig. S3). We then utilized LC3B-GFP to assess the impact of CPU-216 on the formation of LC3 puncta in KBM5-T315I cells (Fig. 6G).

3.7. *CPU-216 induces pyroptosis in T315I-mutant CML cells*

Subsequently, we investigated the mode of cell death induced by CPU-216. Initial RNA-seq analysis revealed alterations in lysosome-related functions following CPU-216 treatment, as indicated by KEGG pathway analysis (Fig. 7A). To monitor lysosomal changes induced by CPU-216, we employed Lysotracker RED, a lysosome-selective live-cell stain. Our findings

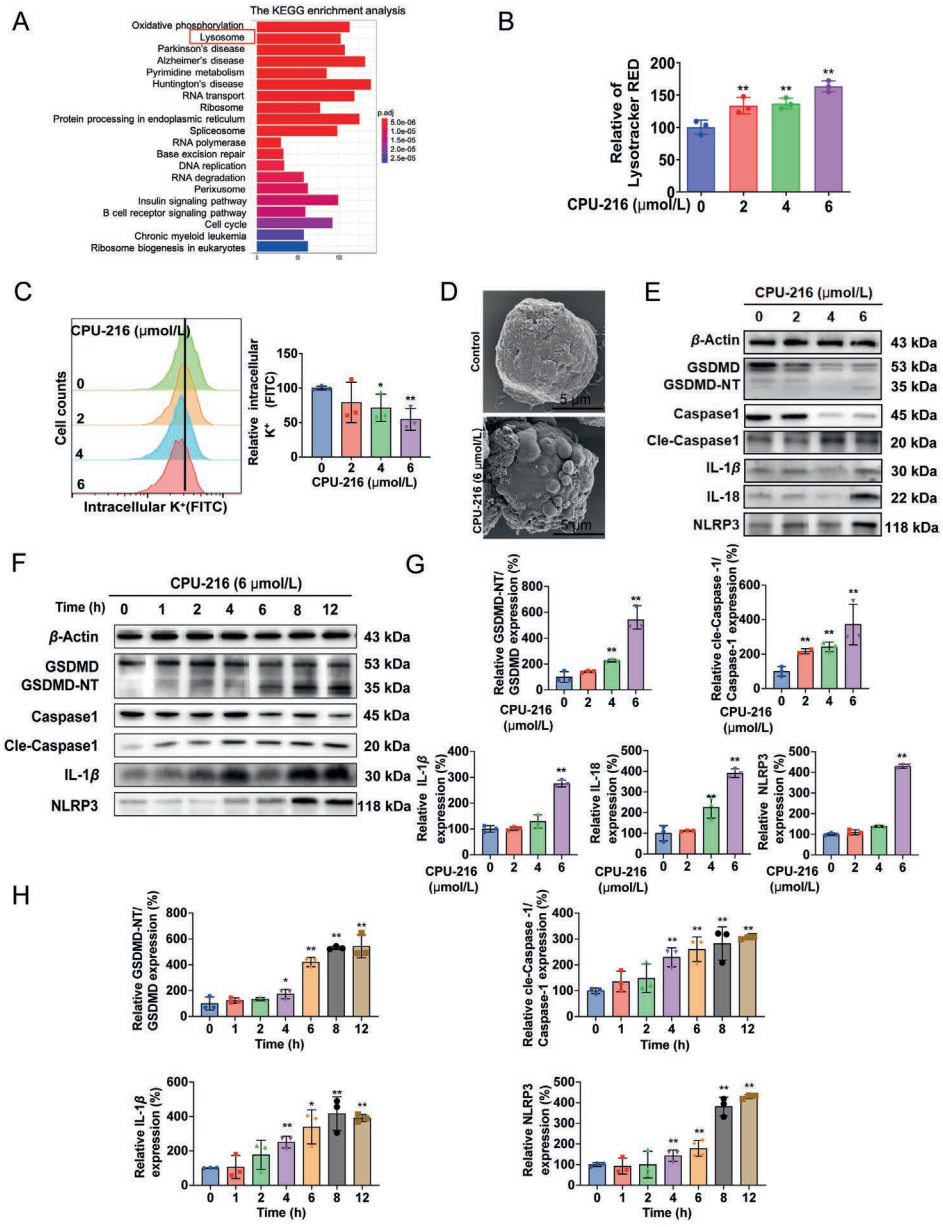

Figure 7 Effects of CPU-216 on lysosomal morphology and pyroptosis in KBM5-T315I cells. (A) KEGG pathway analysis of KBM5-T315I cells after 12 h of treatment with 6 μmol/L CPU-216. (B) Flow cytometric analysis of GEOmean following treatment with 0, 2, 4, 6 μmol/L CPU-216 for 12 h. (C) Flow cytometric analysis of intracellular potassium ion fluorescence intensity and GEOmean statistics in KBM5-T315I cells treated with 0, 2, 4, 6 μmol/L CPU-216 alone or in combination with 3-MA. (D) Scanning electron microscopy was used to observe the morphology of the cell membrane in KBM5-T315I cells after 12 h of treatment with 6 μmol/L CPU-216. (E, G) The effects of 0, 2, 4, 6 μmol/L CPU-216 on the expression of pyroptosis-related proteins Gasdermin D (GSDMD), GSDMD-N-terminal fragment (GSDMD-NT), Caspase-1, IL-1β, and IL-18 in KBM5-T315I cells, β-actin was used as a loading control. (F, H) The impact of 6 μmol/L CPU-216 on the expression of pyroptosis-related proteins GSDMD, Caspase-1, IL-1β in KBM5-T315I cells over time intervals of 0, 1, 2, 4, 6, 8, and 12 h, β-actin was used as a loading control. Error bars: SEM, $n = 3$. Statistical significance of differences in mean values: $^{*}P < 0.05$, $^{**}P < 0.01$.

demonstrated that CPU-216 induced lysosomal enlargement in KBM5-T315I cells (Fig. 7B). Studies suggest that alterations in autophagy and lysosomal function may lead to the efflux of intracellular potassium ions, thereby triggering pyroptosis. Accordingly, we assessed the impact of CPU-216 on intracellular potassium ion levels and found that CPU-216 decreased intracellular K^+ concentrations (Fig. 7C). Subsequently, SEM revealed that KBM5-T315I cells exhibited a morphology resembling fried eggs, characterized by a flattened cytoplasm, indicative of pyroptosis (Fig. 7D). Furthermore, we examined pyroptosis-associated proteins and found elevated ratios of GSDMD-NT/GSDMD and Cle-Caspase-1/Caspase-1 (Fig. 7E–H). As pyroptosis is an inflammatory form of cell death, we also investigated the levels of inflammatory cytokines IL-18 and IL-1β, as well as

the inflammasome component NLRP3, in KBM5-T315I cells. We observed an increase in these inflammatory markers in a time- and dose-dependent manner (Fig. 7E−H).

3.8. In vivo studies demonstrated the anti-T315I-mutant CML activity of CPU-216

Next, we validated the effects of PGK1 inhibitors NG52 (100 mg/kg) and CPU-216 (20 mg/kg) *in vivo*. Initially, NOD/SCID mice were inoculated with KBM5-T315I cells to establish xenograft tumors. On Day 40 post-inoculation, the mice were euthanized, and their tumor volumes were measured. The results demonstrated that both CPU-216 and NG52 were able to reduce tumor volume (Fig. 8A and B). Additionally, we performed immunofluorescence staining on the tumors and observed that both NG52 and CPU-216 increased the expression of the autophagy-related protein LC3B-II and decreased the expression of SQSTM1, while imatinib (100 mg/kg) had minimal effect on LC3B-II and SQSTM1 levels (Fig. 8C and D). We then assessed toxicity to major organs, including the heart, liver, lungs, and kidneys, in the inoculated mice. The results indicated that CPU-216 did not cause significant damage to these organs (Fig. 8E). We also assessed tumor proliferation using Ki-67 staining, which revealed that NG52 and CPU-216 significantly reduced tumor proliferation, whereas imatinib had a lesser effect (Fig. 8F and G). Next, we examined the expression of LC3B-II and SQSTM1 in tumor tissues. The results showed that both NG52 and CPU216 increased LC3B-II expression while decreasing SQSTM1 levels (Fig. 8H). Finally, we measured VCP phosphorylation *in vivo* and found that both CPU-216 and NG52 reduced VCP phosphorylation (Fig. 8I).

Furthermore, to validate the *in vivo* synergy between CPU-216 and imatinib, we established a NOD/SCID mouse model inoculated with KBM5-T315I cells *via* tail vein injection. The mice were treated with imatinib (100 mg/kg), CPU-216 (20 mg/kg), and a combination of imatinib (50 mg/kg) and CPU-216 (10 mg/kg). Splenomegaly, a key indicator of disease progression in CML, was found to be alleviated by imatinib, CPU-216, and their combination in the inoculated mice (Fig. 8J and M). Additionally, the proportion of cells in the blood dramatically decreased in the group treated with the combination of imatinib and CPU-216 in KBM5-T315I-bearing mice, while reductions were less pronounced in groups treated with imatinib or CPU-216 alone (Fig. 8K). Moreover, the combination of imatinib and CPU-216 significantly prolonged the survival of the inoculated mice (Fig. 8L).

4. Discussion

Overcoming TKI resistance in CML, particularly against the recalcitrant T315I mutation, remains a critical therapeutic challenge. Our findings demonstrate that PGK1 overexpression drives survival in T315I-mutated KBM5 cells, and its inhibition significantly restores TKI sensitivity, revealing a promising therapeutic vulnerability in resistant CML.

Clinical trial data (NCT01227135) suggest that in CML patients who have been on imatinib for more than 12 months, the addition of autophagy inhibitors to imatinib therapy improves the 24-month survival rate compared to imatinib monotherapy. Furthermore, after 12 months of combined imatinib and autophagy inhibitor treatment, a reduction of at least 0.5 log in BCR-ABL1 transcript levels is observed[37]. Additionally, the grancalcin (GCA)−TRAF6−ULK1 autophagy regulatory axis has been implicated in imatinib resistance. Silencing heme oxygenase-1 (HO-1) expression in K562-resistant cells resulted in the suppression of autophagy and increased sensitivity to imatinib[38,39].

Overall, the autophagic response to TKIs in multiple tumor types has largely been shown to serve a cytoprotective role, and inhibiting autophagy can reduce TKI resistance. However, in our study, we found that inhibiting PGK1 led to increased autophagy in KBM5-T315I cells and enhanced their sensitivity to TKIs. This finding appears to contradict previous research. Nevertheless, it is important to note that, unlike other tyrosine kinase-driven cancers, CML is a hematologic malignancy primarily driven by the BCR-ABL fusion protein[40]. Autophagy has been shown to be essential for the degradation of BCR-ABL protein. SiRNA-mediated knockdown of autophagy regulators (Beclin 1/ATG7), as well as pharmacological inhibition of autophagy using 3-MA, reduced BCR-ABL/LC3 co-localization in both K562 and CML patient cells[41,42]. Furthermore, imatinib-induced autophagy results from the inhibition of the BCR-ABL−PI3K−AKT−FOXO4−ATF5−mTOR signaling pathway[43]. Therefore, the ability to downregulate BCR-ABL protein levels through the induction of autophagy may represent a crucial mechanism underlying imatinib's therapeutic activity.

Nonetheless, PGK1, as a key enzyme in glycolysis, warrants investigation into its role in CML. This raises the question of how glycolysis may influence autophagy and whether interventions in glucose metabolism could enhance sensitivity to TKIs[44]. Li et al.[45] discovered that 2-deoxyglucose (2-DG), a glucose analog and inhibitor of glucose metabolism, promotes CML cell death by inducing autophagy[45]. The co-treatment with 2-DG and imatinib elicited synergistic inhibitory effects in both the KBM5 and KBM5-T315I cell lines. Our study offers a novel mechanism to explain this phenomenon.

The exploration of PGK1 intervention strategies has become an emerging area of interest. For example, it has been shown that the drug terazosin (TZ) binds to and enhances the activity of the glycolytic enzyme PGK1, thereby increasing ATP levels[46]. He et al.[47] conducted structure-based virtual screening and a series of anticancer pharmaceutical experiments to identify novel small-molecule PGK1-targeted compounds, Z57346765 and CHR-9464. As we know, NG52, a PGK1 inhibitor, also acts as a cell-permeable, reversible, and ATP-competitive inhibitor of the cyclin-dependent kinase Cdc28p, the ortholog of human cyclin-dependent kinase 1 (CDK1), with high structural and mechanistic similarity in their kinase domains. NG52 additionally inhibits the related kinase Pho85p, which is functionally analogous to CDK5. Since CDK1/CDK5 play critical roles in various cancers[48], including CML cells, the use of NG52 as a PGK1 inhibitor inevitably leads to off-target effects. Moreover, CBR-470-1, another PGK1 inhibitor, also functions as a non-covalent nuclear factor erythroid 2-related factor 2 (Nrf2) activator. Nrf2 activation may increase leukemia resistance to cytarabine[49]. Also, there are currently few PGK1 inhibitors approved by the FDA or NMPA. In our study, we performed AI-assisted virtual screening of 20,000 compounds sourced from FDA-approved small molecules and natural compounds. We found that flavonoid compounds exhibited promising PGK1 inhibitory activity, a finding that has rarely been reported. Following this, we retained the flavonoid core and modified its structure, ultimately discovering that CPU-216 effectively inhibits PGK1 and demonstrates a synergistic effect with TKIs. CPU-216 has been approved by the NMPA for clinical trial application (2024LP01723) and is currently undergoing clinical trials in advanced malignant tumors.

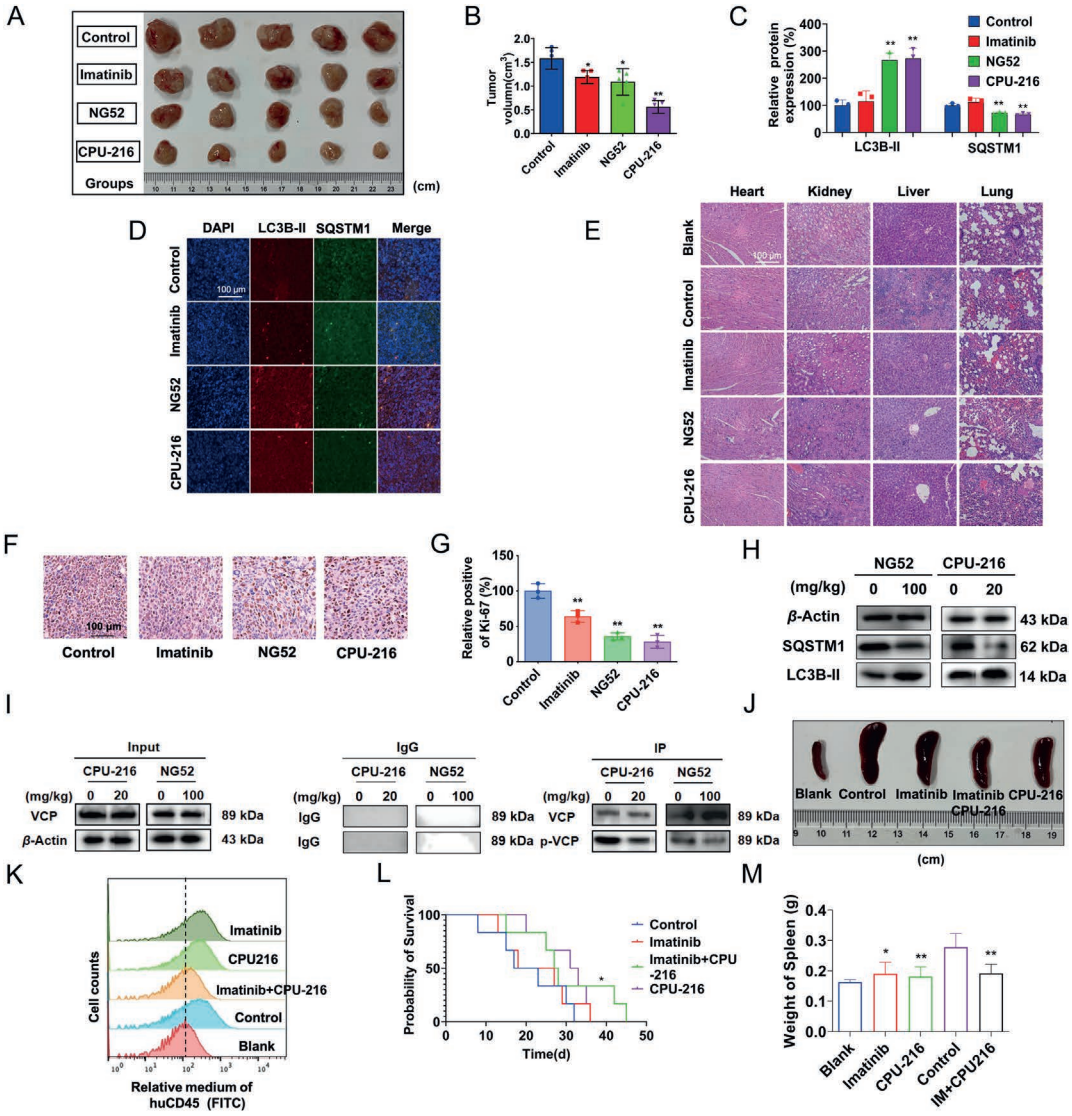

Figure 8 *In vivo* studies demonstrated the anti-T315I-mutant CML activity of CPU-216. (A, B) The effects of imatinib, NG52, and CPU-216 on tumor growth in KBM5-T315I cell-bearing xenograft models were investigated, with measurements of tumor volume (Error bars: SEM, $n = 5$. Statistical significance of differences in mean values: $^{*}P < 0.05$, $^{**}P < 0.01$.). (C, D) The expression of LC3B-II and SQSTM1 in xenograft tumor tissue samples from KBM5-T315I cell-bearing mice was analyzed by immunofluorescence. Green or red fluorescence indicates the expression of LC3 and SQSTM1, respectively, while nuclei were stained with DAPI. Samples were evaluated using a confocal microscope (FV1000; Olympus) with FV10-ASW2.1 acquisition software (Olympus) at room temperature (original magnification 1000 ×; immersion objective 60 × with immersion oil type). (E) Mice were sacrificed after treatment with CPU-216, and their tissues were resected and fixed in 4% formalin for hematoxylin and eosin (H&E) analysis. Images were acquired at 20 × magnification. (F, G) Cell proliferation in KBM5-T315I cells was assessed by Ki-67 staining after treatment with imatinib, NG52, and CPU-216 (Error bars: SEM, $n = 3$. Statistical significance of differences in mean values: $^{*}P < 0.05$, $^{**}P < 0.01$). (H) The expression levels of autophagy-related proteins under the treatment of NG52 and CPU-216. (I) In NG52 or CPU-216-treated tumor tissues, VCP phosphorylation was detected. (J, M) Effects of imatinib, CPU-216, and imatinib plus CPU-216 on the spleen weight in KBM5-T315I cells-bearing NOD/SCID mice were assessed. Representative photographs of the spleens were also displayed. (K) HuCD45 expression was examined in cells from the blood of each group of KBM5-T315I cells-bearing mice by flow cytometry. (L) Kaplan−Meier survival plots for KBM5-T315I cell-bearing NOD/SCID mice were presented (Error bars: SEM, $n \geq 3$, compared with the control group. Statistical significance of differences in mean values: $^{*}P < 0.05$, $^{**}P < 0.01$).

Regarding the induction of cell death in T315I-mutated CML cells, we found that CPU-216 can induce pyroptosis, a form of inflammatory cell death that can significantly influence the immune microenvironment[50]. Given the heterogeneity of CML and the diverse immunosuppressive mechanisms within the tumor microenvironment (TME), relying on a single chemotherapy or immunotherapy approach is unlikely to achieve definitive tumor regression in most patients[51]. Moreover, the TME is typically characterized by immunosuppression, leading to suboptimal responses to conventional immunotherapy[52,53]. Inhibition of PGK1

has been shown to induce pyroptosis, thereby improving the immunosuppressive microenvironment. This suggests that PGK1 inhibition may be linked to immune activation in CML, warranting further investigation.

5. Conclusions

In summary, our study identified that PGK1 is highly expressed in T315I-mutated CML and is associated with malignant proliferation. Inhibiting PGK1 enhances the efficacy of TKIs. PGK1, as a protein kinase, phosphorylates VCP, which in turn inhibits the deubiquitination of Beclin 1. Inhibition of PGK1 induces autophagy in KBM5-T315I cells. Additionally, we screened and synthesized the PGK1 inhibitor CPU-216, which induces autophagy by inhibiting PGK1 and VCP phosphorylation, thereby enhancing the efficacy of TKIs.

Acknowledgements

This work was supported by the National Natural Science Foundation of China (82574638, 82204443), China Postdoctoral Science Foundation (2024M751395), Jiangsu Provincial Health Commission (Z2021064, China), National Natural Science Foundation of China Youth Science Foundation Project Fund supporting Projects of Nanjing University of Chinese Medicine (XPT82204443), Priority Academic Program Development of Jiangsu Higher Education Institutions (Integration of Chinese and Western Medicine, China), the Jiangsu Collaborative Innovation Center of Chinese Medicinal Resources Industrialization. Graphical abstract was created with BioRender.com and published with permission.

Author contributions

Huijing Wang and Fengyu Jiang performed research, analyzed data, and wrote the paper; An Pan and Renjun Gu analyzed data and maintained research data. Yangyang Xue, Chenlong Jin, Wenjie Liu, Yanyu Zhou and Qiuhong Shen provided the preparation and creation of figures. Tonghui Ma and Xiaoxuan Yu conceptualized and financial supported for the project, and directed the experimental design and data analysis.

Conflicts of interest

The authors declare that they have no known competing financial interests or personal relationships that could have appeared to influence the work reported in this paper.

Appendix A. Supporting information

Supporting information to this article can be found online at https://doi.org/10.1016/j.apsb.2025.12.039.

References

1. Hochhaus A, Müller MC, Radich J, Branford S, Hanfstein B, Rousselot P, et al. Dasatinib-associated major molecular responses are rapidly achieved in patients with chronic myeloid leukemia in chronic phase (CML-CP) following resistance, suboptimal response, or intolerance on imatinib. *Blood* 2008;**112**:1095.
2. Ren XM, Pan XF, Zhang Z, Wang DP, Lu XY, Li YP, et al. Identification of GZD824 as an orally bioavailable inhibitor that targets phosphorylated and nonphosphorylated breakpoint cluster region-Abelson (Bcr-Abl) kinase and overcomes clinically acquired mutation-induced resistance against imatinib. *J Med Chem* 2013;**56**:879−94.
3. Hong SS, Kim SJ, Jung KH, Yan HH, Ryu JS. Abstract 5389: novel kinase inhibitor for imatinib-resistant chronic myeloid leukemia with T315I mutation. *Cancer Res* 2015;**75**:5389.
4. Hochhaus A, O'brien SG, Guilhot F, Druker BJ, Branford S, Foroni L, et al. Erratum: six-Year follow-up of patients receiving imatinib for the first-line treatment of chronic myeloid leukemia. *Leukemia* 2010;**24**:1102.
5. Chan O, Talati C, Isenalumhe L, Shams S, Nodzon L, Fradley M, et al. Side-effects profile and outcomes of ponatinib in the treatment of chronic myeloid leukemia. *Blood Adv* 2020;**4**:530−8.
6. Shanmuganathan N, Hughes T. Accelerated-phase CML: *de novo* and transformed. *Hematology Am Soc Hematol Educ Program* 2023;**2023**:459−68.
7. Liu J, Zhang Y, Huang HL, Lei XY, Tang GT, Cao X, et al. Recent advances in bcr-abl tyrosine kinase inhibitors for overriding T315I mutation. *Chem Biol Drug Des* 2021;**97**:649−64.
8. Quintas-Cardama A, Cortes J. Therapeutic options against BCR-ABL1 T315I-positive chronic myelogenous leukemia. *Clin Cancer Res* 2008;**14**:4392−9.
9. Mccarrey JR, Thomas K. Human testis-specific PGK gene lacks introns and possesses characteristics of a processed gene. *Nature* 1987;**326**:501−5.
10. Nie H, Ju H, Fan J, Shi X, Cheng Y, Cang X, et al. *O*-GlcNAcylation of PGK1 coordinates glycolysis and TCA cycle to promote tumor growth. *Nat Commun* 2020;**11**:36.
11. Liang C, Shi S, Qin Y, Meng Q, Hua J, Hu Q, et al. Localisation of PGK1 determines metabolic phenotype to balance metastasis and proliferation in patients with SMAD4-negative pancreatic cancer. *Gut* 2020;**69**:888−900.
12. Liao L, Dang W, Lin T, Yu J, Liu T, Li W, et al. A potent PGK1 antagonist reveals PGK1 regulates the production of IL-1β and IL-6. *Acta Pharm Sin B* 2022;**12**:4180−92.
13. Pontén F, Schwenk JM, Asplund A, Edqvist PH. The human protein atlas as a proteomic resource for biomarker discovery. *J Intern Med* 2011;**270**:428−46.
14. Li XJ, Jiang YH, Meisenhelder J, Yang WW, Hawke DH, Zheng YH, et al. Mitochondria-translocated PGK1 functions as a protein kinase to coordinate glycolysis and the TCA cycle in tumorigenesis. *Mol Cells* 2016;**61**:705−19.
15. Le Y, Zhang QY, Xie SS, Cheng Z, Li RJ, Zhu HK, et al. HDAC inhibitor chidamide overcomes drug resistance in chronic myeloid leukemia with the T315i mutation through the Akt-autophagy pathway. *Hum Cell* 2023;**36**:1564−77.
16. He W, Liu ST, Wei W, Qin R, Jinfeng T, Tan JF, et al. mTOR inhibition by AZD2014 alleviates BCR::ABL1 independent imatinib resistance through enhancing autophagy in CML resistant cells. *Am J Cancer Res* 2024;**14**:2770−89.
17. Willig JB, deCouto NM, Vianna D, Mariot C da S, Gnoatto SC, Buffon A, et al. Betulinic acid−brosimine B hybrid compound has a synergistic effect with imatinib in chronic myeloid leukemia cell line, modulating apoptosis and autophagy. *Pharmaceuticals* 2023;**16**:586.
18. Meyer H, Weihl CC. The VCP/p97 system at a glance: connecting cellular function to disease pathogenesis. *J Cell Sci* 2014;**127**:3877−83.
19. Xia D, Tang WK, Ye Y. Structure and function of the AAA+ ATPase p97/Cdc48p. *Gene* 2016;**583**:64−77.
20. Singh AN, Oehler J, Torrecilla I, Kilgas S, Ramadan K. The p97−Ataxin 3 complex regulates homeostasis of the DNA damage response E3 ubiquitin ligase RNF 8. *EMBO J* 2019;**38**:e102361.
21. Wrobel L, Hill SM, Ashkenazi A, Rubinsztein DC. VCP/p97 modulates PtdIns3P production and autophagy initiation. *Autophagy* 2021;**17**:1052−3.
22. Ganji R, Mukkavalli S, Somanji F, Raman M. The VCP−UBXN1 complex mediates triage of ubiquitylated cytosolic proteins bound to the BAG6 complex. *Mol Cell Biol* 2018;**38**:e00154.

23. Ju JS, Fuentealba RA, Miller SE, Jackson E, Piwnica-Worms D, Baloh RH, et al. Valosin-containing protein (VCP) is required for autophagy and is disrupted in VCP disease. *J Cell Biol* 2009;**187**: 875−88.
24. Yeo BK, Hong CJ, Chung KM, Woo H, Kim K, Jung S, et al. Valosin-containing protein is a key mediator between autophagic cell death and apoptosis in adult hippocampal neural stem cells following insulin withdrawal. *Mol Brain* 2016;**9**:31.
25. Chung KM, Park H, Jung S, Ha S, Yoo SJ, Woo H, et al. Calpain determines the propensity of adult hippocampal neural stem cells to autophagic cell death following insulin withdrawal. *Stem Cell* 2015; **33**:3052−64.
26. Yu X, Li H, Hu P, Qing Y, Wang X, Zhu M, et al. Natural HDAC-1/8 inhibitor baicalein exerts therapeutic effect in CBF-AML. *Clin Transl Med* 2020;**10**:e154.
27. Qi J, Singh S, Hua WK, Cai Q, Chao SW, Li L, et al. HDAC8 inhibition specifically targets Inv(16) acute myeloid leukemic stem cells by restoring p53 acetylation. *Cell Stem Cell* 2015;**17**:597−610.
28. Hsu MC, Hung WC. Pyruvate kinase M2 fuels multiple aspects of cancer cells: from cellular metabolism, transcriptional regulation to extracellular signaling. *Mol Cancer* 2018;**17**:35.
29. Zhang T, Wang Y, Yu H, Zhang T, Guo L, Xu J, et al. PGK1 represses autophagy-mediated cell death to promote the proliferation of liver cancer cells by phosphorylating PRAS40. *Cell Death Dis* 2022;**13**:68.
30. Zhu K, Cai Y, Si X, Ye Z, Gao Y, Liu C, et al. The phosphorylation and dephosphorylation switch of VCP/p97 regulates the architecture of centrosome and spindle. *Cell Death Differ* 2022;**29**:2070−88.
31. Egerton M, Samelson LE. Biochemical characterization of valosin-containing protein, a protein tyrosine kinase substrate in hematopoietic cells. *J Biol Chem* 1994;**269**:11435−41.
32. Zhang SH, Liu J, Kobayashi R, Tonks NK. Identification of the cell cycle regulator VCP (p97/CDC48) as a substrate of the band 4.1-related protein-tyrosine phosphatase PTPH1. *J Biol Chem* 1999;**274**:17806−12.
33. Klein JB, Barati MT, Wu R, Gozal D, Sachleben Jr LR, Kausar H, et al. Akt-mediated valosin-containing protein 97 phosphorylation regulates its association with ubiquitinated proteins. *J Biol Chem* 2005;**280**:31870−81.
34. Ali NA, Wu J, Hochgräfe F, Chan H, Nair R, Ye S, et al. Profiling the tyrosine phosphoproteome of different mouse mammary tumour models reveals distinct, model-specific signalling networks and conserved oncogenic pathways. *Breast Cancer Res* 2014;**16**:437.
35. Villén J, Beausoleil SA, Gerber SA, Gygi SP. Large-scale phosphorylation analysis of mouse liver. *Proc Natl Acad Sci U S A* 2007;**104**: 1488−93.
36. Mori-Konya C, Kato N, Maeda R, Yasuda K, Higashimae N, Noguchi M, et al. p97/valosin-containing protein (VCP) is highly modulated by phosphorylation and acetylation. *Genes Cells* 2009;**14**:483−97.
37. Horne GA, Stobo J, Kelly C, Mukhopadhyay A, Latif AL, Dixon-Hughes J, et al. A randomised phase II trial of hydroxychloroquine and imatinib *versus* imatinib alone for patients with chronic myeloid leukaemia in major cytogenetic response with residual disease. *Leukemia* 2020;**34**:1775−86.
38. Han SH, Korm S, Han YG, Choi SY, Kim SH, Chung HJ, et al. GCA links TRAF6−ULK1-dependent autophagy activation in resistant chronic myeloid leukemia. *Autophagy* 2019;**15**:2076−90.
39. Cao L, Wang J, Ma D, Wang P, Zhang Y, Fang Q. Heme oxygenase-1 contributes to imatinib resistance by promoting autophagy in chronic myeloid leukemia through disrupting the mTOR signaling pathway. *Biomed Pharmacother* 2016;**78**:30−8.
40. Sawyers CL. Chronic myeloid leukemia. *N Engl J Med* 1999;**340**: 1330−40.
41. Baukje ME, Michelle JN, Lisa CC, Tracey RO, Mary RC, Sharon LM. Induction of autophagy by imatinib sequesters bcr-abl in autophagosomes and down-regulates bcr-abl protein. *Am J Hematol* 2013;**88**: 455−62.
42. Jiang L, Wang Y, Li Q, Tu Z, Zhu S, Tu S, et al. Design, synthesis, and biological evaluation of bcr-abl PROTACs to overcome T315I mutation. *Acta Pharm Sin B* 2021;**11**:1315−28.
43. Sheng Z, Ma L, Sun JE, Zhu LJ, Green MR. BCR-ABL suppresses autophagy through ATF5-mediated regulation of mTOR transcription. *Blood* 2011;**118**:2840−8.
44. Lu Z, Hunter T. Metabolic kinases moonlighting as protein kinases. *Trends Biochem Sci* 2018;**43**:301−10.
45. Li Y, Zeng P, Xiao J, Huang P, Liu P. Modulation of energy metabolism to overcome drug resistance in chronic myeloid leukemia cells through induction of autophagy. *Cell Death Discov* 2022;**8**:212.
46. Riley MJ, Mitchell CC, Ernst SE, Taylor EB, Welsh MJ. A model for stimulation of enzyme activity by a competitive inhibitor based on the interaction of terazosin and phosphoglycerate kinase 1. *Proc Natl Acad Sci U S A* 2024;**121**:e2318956121.
47. He Y, Luo Y, Huang L, Zhang D, Hou H, Liang Y, et al. Novel inhibitors targeting the PGK1 metabolic enzyme in glycolysis exhibit effective antitumor activity against kidney renal clear cell carcinoma *in vitro* and *in vivo*. *Eur J Med Chem* 2024;**267**:116209.
48. Tóth O, Rácz GA, Oláh E, Tóth M, Szabó E, Várady G, et al. Identification of new reference genes with stable expression patterns for cell cycle experiments in human leukemia cell lines. *Sci Rep* 2025;**15**:1052.
49. Hu T, Pan C, Zhang T, Ni M, Wang W, Zhang S, et al. Retraction note: nrf2 overexpression increases the resistance of acute myeloid leukemia to cytarabine by inhibiting replication factor C4. *Cancer Gene Ther* 2025;**32**:739.
50. Zhang W, Wu H, Liao Y, Zhu C, Zou Z. Caspase family in autoimmune diseases. *Autoimmun Rev* 2024;**24**:103714.
51. Jiang F, Liu W, Zhou Y, Lin S, Zhang Q, Zhang W, et al. Bortezomib induces cell apoptosis and increases the efficacy of αPD-1 in BCR:: ABL T315I mutation CML by targeting UBE2Q1. *Int immunopharmacol* 2024;**143**:113311.
52. Dawson A, Zarou M, Prasad B, Bittencourt-Silvestre J, Zerbst D, Himonas E, et al. Leukaemia exposure alters the transcriptional profile and function of BCR::ABL1 negative macrophages in the bone marrow niche. *Nat Commun* 2024;**15**:1090.
53. Choi D, Tremblay D, Iancu-Rubin C, Mascarenhas J. Programmed cell death-1 pathway inhibition in myeloid malignancies: implications for myeloproliferative neoplasms. *Ann Hematol* 2017;**96**:919−27.